



# Impact of power-law rheology on the viscoelastic relaxation pattern and afterslip distribution following the 2010 Mw 8.8 Maule earthquake

Carlos Peña<sup>a,b,\*</sup>, Oliver Heidbach<sup>a</sup>, Marcos Moreno<sup>c,e</sup>, Jonathan Bedford<sup>a</sup>, Moritz Ziegler<sup>a</sup>, Andrés Tassara<sup>d,e</sup>, Onno Oncken<sup>a,b</sup>

<sup>a</sup> Helmholtz Centre Potsdam, GFZ German Research Centre for Geosciences, Potsdam, Germany

<sup>b</sup> Institute of Geological Sciences, Freie Universität Berlin, Berlin, Germany

<sup>c</sup> Departamento de Geofísica, Facultad de Ciencias Físicas y Matemáticas, Universidad de Concepción, Concepción, Chile

<sup>d</sup> Departamento de Ciencias de la Tierra, Facultad de Ciencias Químicas, Universidad de Concepción, Concepción, Chile

<sup>e</sup> Millenium Nucleus CYCLO "The Seismic Cycle along Subduction Zones", Chile

## ARTICLE INFO

### Article history:

Received 11 November 2019

Received in revised form 8 April 2020

Accepted 17 April 2020

Available online xxxx

Editor: J.-P. Avouac

### Keywords:

2010 Maule earthquake  
postseismic deformation  
numerical modelling  
afterslip  
power-law rheology  
GPS

## ABSTRACT

After large earthquakes at subduction zones, the plate interface continues moving due to mostly frictional afterslip or simply afterslip processes. Below approximately 60 km depth, the seismic moment release at the plate interface is quite small indicating that the shear strength is low and stable sliding is the prevailing process. This agrees with the lack of significant interseismic locking at deeper segments (>60 km) resulting from the inversion of geodetic data and thus low afterslip can be expected. However, inversion models that employ linear viscoelastic mantle rheology and an elastic crust result in significant afterslip at depths >60 km. In this paper, we present a combination of a 3D forward geomechanical model with power-law rheology that simulates postseismic relaxation with dislocation creep processes in the crust and upper mantle and an afterslip inversion. We estimate the cumulative viscoelastic relaxation and the afterslip distribution for the first six years following the 2010 Mw 8.8 Maule earthquake in Chile. The cumulative afterslip distribution is obtained from the inversion of the residual surface displacements between the observed displacements from the continuous GPS (cGPS) and the ones from the forward modelling. We investigate five simulations, four with different dislocation creep parameters for the crust, slab, and upper mantle and one with elastic properties for the crust and slab, and a linear viscoelastic upper mantle for comparison. Our preferred simulation considers a weak crust since it shows the best fit to the cumulative cGPS postseismic displacements, a good fit to the time-series, and, in particular, a good spatial correlation between afterslip and aftershock activity. In this simulation, most of the viscoelastic relaxation occurs in the continental lower crust beneath the volcanic arc due to dislocation creep processes. The resulting afterslip pattern from the inversion is reduced at depths >60 km, which correlates to the low cumulative seismic moment that is released from aftershocks at these depths. Furthermore, the cumulative afterslip moment release from this simulation corresponds to 10% of the main shock in six years, which is approximately half of the moment release that results from models with an elastic crust and linear viscosity in the upper mantle. We conclude that an integrated analysis by considering power-rheology with dislocation creep processes in the continental crust and upper mantle along with aftershock activity may be used to constrain location and magnitude postseismic relaxation processes better.

© 2020 Elsevier B.V. All rights reserved.

## 1. Introduction

In the years following large magnitude earthquakes, the surface deformation is transient and occurs at high and variable rates, generally decaying with time. This postseismic deformation is a

superposition of afterslip at the plate interface which seems to surround the plate interface regions that had the largest coseismic slip (Bedford et al., 2013; Hsu et al., 2006; Perfettini and Avouac, 2007; Perfettini et al., 2010), poroelastic rebound in the oceanic and continental crust (Hu et al., 2014; Masterlark, 2003) and viscoelastic relaxation of co-seismically induced differential stresses in the continental crust and upper mantle (Freed and Bürgmann, 2004; Freed et al., 2017; Hergert and Heidbach, 2006; Peña et al., 2019; Qiu et al., 2018; Sun et al., 2014; Wang et al., 2012). The

\* Corresponding author at: Helmholtz Centre Potsdam, GFZ German Research Centre for Geosciences, Potsdam, Germany.

E-mail address: carlosp@gfz-potsdam.de (C. Peña).

contribution of poroelastic rebound is small compared to afterslip and viscoelastic relaxation processes, but the relative contribution of the latter two processes is not clear and strongly depends on the incorporated model rheology.

Afterslip distribution following earthquakes has been usually investigated using linear inversion and, to a lesser extent, self-consistent stress-driven approaches that model the observed post-seismic cGPS surface displacements. The existing models are quite different and consider fully elastic rheology (Aguirre et al., 2019; Bedford et al., 2013; Perfettini et al., 2010), use the residual between the surface postseismic displacements and the results from a forward model of the postseismic relaxation with linear viscoelastic rheology (Bedford et al., 2016; Freed et al., 2017), or consider the afterslip-viscoelastic coupling with linear and non-linear viscoelastic relaxation processes (Agata et al., 2019; Barbot, 2018; Lambert and Barbot, 2016; Masuti et al., 2016; Muto et al., 2019; Qiu et al., 2018; Rollins et al., 2015; Rousset et al., 2012; Shi et al., 2020; Tsang et al., 2016; Yamagiwa et al., 2015). At subduction zones, these models showed that generally afterslip dominates near field and viscoelastic processes far field, but the use of close-to-trench GPS observations after the 2011 Tohoku-oki earthquake, Japan, revealed that viscoelastic relaxation in the oceanic mantle may also contribute considerably to the near field signal (Freed et al., 2017; Sun et al., 2014; Agata et al., 2019). Yet, the contribution of afterslip and viscoelastic relaxation processes to the surface deformation field cannot easily be distinguished based on near-field and far-field cGPS observations (Weiss et al., 2019). The incorporation of viscoelastic relaxation processes in the mantle reduces the deep afterslip and increases the shallow afterslip compared to a model with fully elastic properties (Qiu et al., 2018; Tsang et al., 2016; Sun et al., 2014). Nevertheless, even with the inclusion of viscoelastic relaxation in the upper mantle, these model settings generally result in considerable afterslip at depths >60 km from the inversion. For instance, the afterslip model of Yamagiwa et al. (2015) results in afterslip of ~2 m at 80 km depth after 2.5 years of the 2011 Tohoku-oki earthquake in Japan. Similar results were found in the Sumatra-Andaman region with afterslip values of ~1.5–3 m at the same depth by Tsang et al. (2016) and Qiu et al. (2018).

However, large afterslip at depths >60 km is apparently not in agreement with frictional properties and shear strength of the megathrust inferred from seismic wave radiation (Lay et al., 2012), friction laws (Agata et al., 2019; Avouac, 2015), and the low aftershock activity (Agurto-Detzel et al., 2019; Lange et al., 2012, 2014; Lay et al., 2012). Recently, Agata et al. (2019) combined a model with stress-driven afterslip considering laboratory-derived friction laws and non-linear rheology for the upper mantle. Their results indicate that afterslip mainly occurs at depth <60 km after 2.8 years of the 2011 Tohoku-oki earthquake in Japan. This depth is in the temperature range of 300–450 °C for the Tohoku-oki region, Japan (Wada et al., 2015), which represents the onset of brittle-ductile transition (Scholz, 1988), i.e., the down-dip limit of the seismogenic zone. Nevertheless, this transition varies among subduction zones (Oleskevich et al., 1999; Shi et al., 2020), mainly because of age and velocity of the incoming plate (Oleskevich et al., 1999; Völker et al., 2011). On the other hand, geodetic inter-seismic locking (Avouac, 2015; Li et al., 2018; Loveless and Meade, 2010; Métis et al., 2012; Moreno et al., 2010) indicates that the down-dip limit of the seismogenic zone is approximately 50 km at most subduction zones.

The distribution of afterslip following the 2010  $M_w$  8.8 Maule earthquake in Chile has been investigated in a number of studies, each using different elastic and viscoelastic model configurations (Aguirre et al., 2019; Bedford et al., 2013, 2016; Klein et al., 2016; Lin et al., 2013; Peña et al., 2019; Weiss et al., 2019). Results from each study differ significantly indicating that the incorporated

model rheology for the upper mantle and continental crust has a major impact on the afterslip distribution at the plate interface. For example, models that use an elastic rheology for the crust and mantle result in afterslip with a maximum of up to 2 m mainly between 25–50 km depth, but also significant afterslip at depths >60 km (Bedford et al., 2013; Lin et al., 2013). The study of Klein et al. (2016) uses a model with Burgers rheology with a linear viscosity of  $4.75 \times 10^{18}$  Pa s for the upper mantle below an elastic crust. They also include a deep subduction channel with viscosities close to  $10^{17}$  Pa s at depths between 55–135 km, limiting the afterslip distribution to a shallower region (<55 km depth) with a maximum of ~9 m over the first year. Weiss et al. (2019) used a model that jointly inverts for viscous strain in the continental lower crust and upper mantle and afterslip at the plate interface. Their maximum afterslip is up to 8 m and mostly concentrated in the vicinity of the trench at >20 km depth, while viscoelastic relaxation in the lower crust has little impact of the postseismic signal at the surface. In contrast, Peña et al. (2019) showed that stress relaxation in the continental lower crust due to non-linear dislocation creep processes reduces the maximum afterslip to ~1 m and shift it to deeper regions between 20–35 km depths. However, their work is a semi-generic study using a 2D geomechanical forward model in which the afterslip distribution is pre-defined as a boundary condition rather than an inversion to explain residual GPS postseismic surface displacements. A 3D model for the Maule postseismic deformation that accounts for dislocation creep processes in a forward sense and then obtains the afterslip distribution on the plate interface from the residual displacements between the observed and the viscoelastic forward simulation is still missing. The postseismic deformation associated to the Maule event has important deformation features along-strike (Bedford et al., 2013; Klein et al., 2016; Li et al., 2017); therefore, a 3D model may give a more integrated understanding of the driven processes rather than a 2D approach that assumes plain strain in the along-strike direction.

Thus, in this study we extend the 2D model of Peña et al. (2019) into a 3D model using a power-law rheology with dislocation creep for the crust and upper mantle. Furthermore, we now combine the postseismic forward modelling of viscoelastic relaxation with a standard linear inversion to estimate the cumulative afterslip distribution on the plate interface six years after the main shock. We use the observed surface displacements from 55 cGPS stations as shown in Fig. 1. Our primary goal is to investigate the impact of rheology (linear and power-law) on the inverted afterslip distribution using a range of plausible dislocation creep parameters for the continental crust and the upper mantle, as well as the linear rheology case (elastic crust and linear viscoelastic mantle). Our results show that the moment release by afterslip is 10–14% of the main shock. Furthermore, we find that simulations that result in viscous deformation in the continental lower crust concentrate the afterslip to depths <60 km. The afterslip distribution from our preferred simulation is chosen from its lowest residual between the observed and simulated surface displacements as well as its good correlation with the accumulated moment release from the aftershocks at the plate interface.

## 2. Model set up and cGPS data

We estimate the afterslip distribution on the plate interface with a combination of a 3D geomechanical forward model and an inversion approach (Fig. 2). The 3D viscoelastic forward model describes the postseismic relaxation for the first six years after the 2010 Maule  $M_w$  8.8 earthquake using linear and power-law rheology. The resulting cumulative predicted surface displacements are subtracted from the observed displacements at the cGPS stations in the model area. After that, the cumulative residual displacements

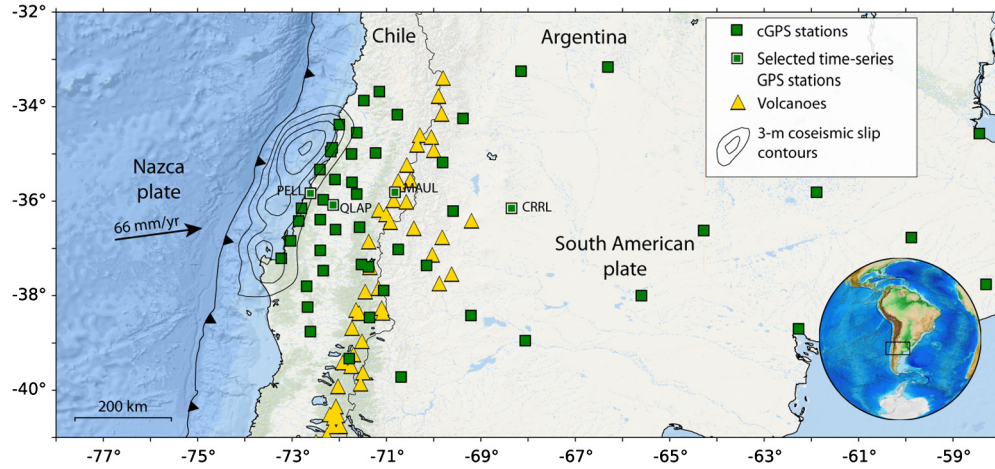


**Fig. 1.** Study area with location of cGPS stations used in this study. Grey contour lines depict the area of coseismic slip of the 2010 Maule earthquake taken from Moreno et al. (2012). Stations shown by a white border and their station names are the ones to be compared with displacement time series from the model results (see Fig. 5).

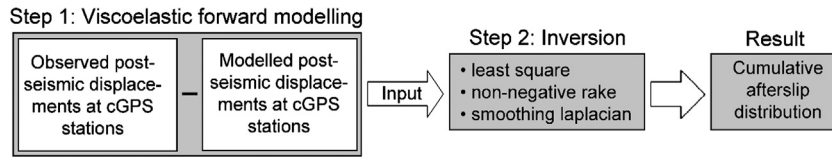


**Fig. 2.** Sketch of the model workflow that combines a forward model of the postseismic viscoelastic relaxation with an inversion for the cumulative afterslip distribution at the plate interface six years after the main shock. The input of the inversion model is the residual between the cumulative postseismic displacements at the cGPS stations and the results of the forward simulation at the cGPS stations after six years.

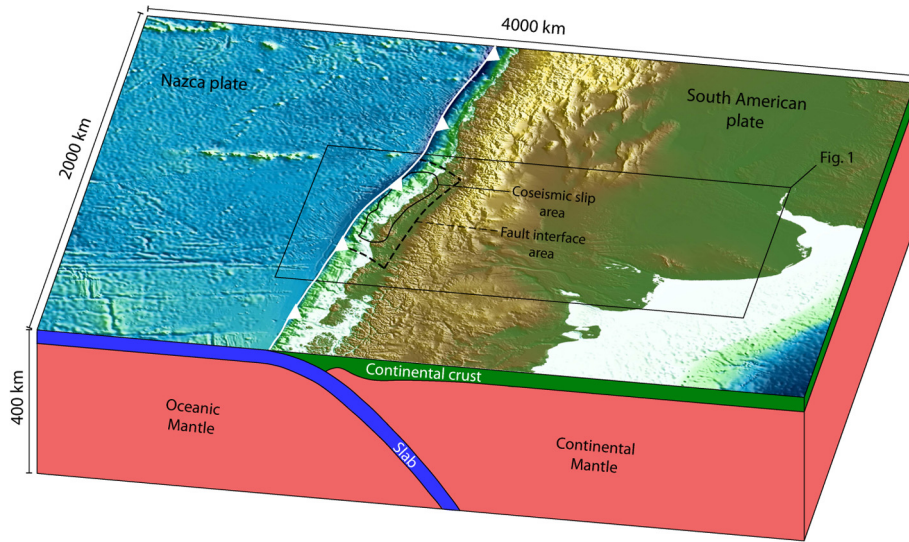


**Fig. 3.** Model geometry and study area with twofold exaggeration in vertical direction. At the lateral and lower model boundary normal displacements are not allowed while the surface is free of constraints. Assigned coseismic slip greater than 3 m is shown by black solid contour lines; dashed rectangular box indicates the domain of the afterslip inversion on the fault interface. Rectangular box shows the location of the study area presented in Fig. 1.

are used in a linear inversion to finally estimate the afterslip at the plate interface. More details on the two models and the cGPS data are presented in the two following subsections.

### 2.1. Set up of the forward model

The model geometry of the forward model to describe the viscoelastic relaxation includes the slab from Hayes et al. (2012) and the Moho from Tassara et al. (2006). It extends 4000 km in West-East direction, 2000 km in North-South and 400 km in the vertical direction (Fig. 3). This size is large enough to avoid artefacts that result from the model boundary conditions.

At steady state, and under high-temperature and high-pressure conditions, rocks deform predominantly due to dislocation creep processes described by equation:

$$\dot{\epsilon} = A\sigma^n \exp\left(\frac{-Q}{RT}\right) \quad (1)$$

While a linear viscoelastic material with effective viscosity ( $\eta$ ) deforms as:

$$\dot{\epsilon} = \frac{\sigma}{2\eta} \quad (2)$$

where  $\dot{\epsilon}$  is the strain rate,  $A$  is a pre-exponent parameter,  $\sigma$  is the differential stress,  $n$  is the stress exponent,  $Q$  is the activa-



**Table 1**  
Elastic properties and dislocation creep parameters.

Rock type <sup>b</sup>	Young's modulus E (GPa) <sup>a</sup>	Poisson's ratio $\nu^a$	Pre-exponent A (MPa <sup>-n</sup> s <sup>-1</sup> ) <sup>b</sup>	Stress exponent $n^b$	Activation energy Q (kJ mol <sup>-1</sup> ) <sup>b</sup>
Wet quartzite	100	0.265	$3.2 \times 10^{-4}$	2.3	154
Wet olivine 1*	160	0.25	$5.6 \times 10^6$	3.5	480
Wet olivine 2*	160	0.25	$1.6 \times 10^5$	3.5	480
Diabase	120	0.3	$2.0 \times 10^{-4}$	3.4	260

<sup>a</sup> Reference source from Christensen (1996) and Moreno et al. (2012).

<sup>b</sup> Reference source from Hirth and Kohlstedt (2003), Ranalli (1997)

\* Wet olivine 1 and 2 contain 0.1 and 0.005% of water, respectively.

tion energy for creep,  $R$  is the gas constant and  $T$  is the absolute temperature (Freed and Bürgmann, 2004; Hirth and Kohlstedt, 2003; Masuti et al., 2016; Wang et al., 2012). Studies from laboratory experiments in lithospheric rocks (Carter and Kirby, 1978; Chopra, 1997) and postseismic deformation following large-magnitude earthquakes (Agata et al., 2019; Freed et al., 2012; Masuti et al., 2016) suggest a more rapid initial transient deformation than the one from the power-law formulation in equation (1). Here, we neglect this rapid initial transient response since its impact is small in comparison to the large uncertainty that result from the temperature models (Ranalli, 1997; Völker et al., 2011) and creep parameters (Hirth and Kohlstedt, 1996, 2003; Ranalli, 1997). We thus model the viscoelastic relaxation with power-law and linear rheology using equations (1) and (2), respectively. Details on the rock properties are presented in section 2.4. The temperature field for our model is adopted from Völker et al. (2011). Since the domain of this temperature model is 2D only and laterally smaller than ours, we first take the isotherms at the borders of the temperature model and extend them to our model's boundaries. This assumption is justified as there are no relevant changes in the slab geometry and age in the key postseismic deformation area, which are controlling factors in the thermal structure (e.g., Völker et al., 2011). Finally, we interpolate the temperature field and assign the corresponding temperature to each node in the 3D model domain (Fig. S1). We assume that the implemented temperature field is time-independent because no significant changes are expected during our model time of six years.

At the lateral and bottom model boundaries displacement is only allowed in a boundary-parallel direction; the model surface is free of constraints. To initiate the postseismic deformation we simulate the coseismic rupture of the Maule  $M_w$  8.8 earthquake on a fault that is  $\sim 700$  km long in strike direction and  $\sim 90$  km deep. The relative displacement of the hanging and foot walls is governed by linear constraint equations that satisfy the specified slip at each node-pair (Freed et al., 2017; Masterlark, 2003). Here, we apply the coseismic slip of Moreno et al. (2012) as displacement boundary conditions. We employ this slip model because we use the same elastic material properties and model geometry as implemented in the model of Moreno et al. (2012). The resulting coseismic deformation is consistent with the observed coseismic deformation at the GPS stations (Fig. S2).

Since power-law rheology is stress dependent, we evaluate the effects of background stresses with the 2D model of Peña et al. (2019). We find no substantial differences in the cumulative six-years postseismic displacements (Fig. S3 and S4); therefore we assume in the following that background stresses can be disregarded. Thus, the differential stress changes imposed by the coseismic slip cause the onset of the dislocation creep processes with rates depending on the dislocation creep parameters. The model volume is discretized into 2,350,000 finite elements with high resolution close to the area of key postseismic deformation ( $\sim 5$  km) and significant coarser resolution ( $\sim 50$  km) at the model boundaries where no deformation is expected. The resulting numerical

problem is solved with the commercial finite element software ABAQUS<sup>TM</sup>, version 6.11.

## 2.2. Continuous GPS data

The postseismic deformation associated with the 2010  $M_w$  8.8 Maule earthquake in Chile was well recorded by a rapid international collaborative effort under which 67 cGPS stations were installed (e.g., Vigny et al., 2011). We use the first six-years of the postseismic surface displacements observed by cGPS as reported by Li et al. (2017). In this data set, the cumulative surface displacements at cGPS stations are obtained from daily solutions processed at Nevada Geodetic Laboratory (University of Nevada, U.S., Blewitt et al., 2018), where the cGPS time series are processed in the IGS08 reference frame (Rebischung et al., 2012). Li et al. (2017) considered only stations with more than 4 years of temporal coverage, obtaining a total of 55 cGPS stations that fulfill this criterion. Furthermore, they applied the trajectory model of Bevis and Brown (2014) and removed the effect of seasonal variations, aftershock and/or jump signals. We also removed the secular component by identifying the interseismic displacements at each postseismic GPS stations from previous studies (Métois et al., 2012; Moreno et al., 2010).

## 2.3. Afterslip inversion

The input for the inversion model of the afterslip is the residual between the results of the forward model of the cumulative postseismic relaxation after six years and the cGPS data as described in Fig. 2. We use this residual signal to invert for the afterslip distribution by calculating the Green's functions at each node-pair using linear equations that satisfy the static dislocation of node-pairs by imposing kinematic constraints as described by Masterlark (2003). Following the approach from previous studies considering forward simulation for the viscoelastic response and an inversion for the afterslip (e.g., Bedford et al., 2016; Freed et al., 2017), the Green's functions for the afterslip inversion are calculated from the 3D model by considering only the elastic material properties stated in Table 1. The inverse problem is solved with a least squares method, a non-negative rake varying from 0 to 180° (i.e., afterslip in down-dip direction is not allowed), and Laplacian smoothing constraints that minimize the differences among neighboring node-pair dislocations (e.g. Bedford et al., 2016; Freed et al., 2017). Here, the smoothing constants are chosen from the trade-off curve between the residual norm and the solution length (Bedford et al., 2016; Moreno et al., 2012; Masterlark, 2003) (more information in Fig. S8).

Our approach implies that afterslip and viscous relaxation are assumed to act independently from each other. However, the rate and magnitude of afterslip will indeed change the stress state, potentially affecting the viscous response. To investigate this, we combined afterslip and power-law rheology and compare the results to assess to what extent these processes are coupled. In the first case, we use the 3D model to jointly simulate six-year

**Table 2**  
Configuration of simulations.

Simulation	Rheology	Continental crust	Continental mantle	Slab	Oceanic mantle
PL1	Power-law	Wet quartzite	Wet olivine 1	Diabase	Wet olivine 2
PL2	Power-law	Wet quartzite	Wet olivine 2	Diabase	Wet olivine 2
PL3	Power-law	Diabase	Wet olivine 1	Diabase	Wet olivine 2
PL4	Power-law	Diabase	Wet olivine 2	Diabase	Wet olivine 2
LI5	Linear Maxwell	Elastic*	$1.3 \times 10^{19}$ Pa s	Elastic*	$1.3 \times 10^{19}$ Pa s

\* Elastic properties (Young's modulus and Poisson's ratio) for the continental crust and slab as described in Table 1 for wet quartzite and diabase, respectively.

postseismic deformation with the afterslip and rheology from our preferred simulation. In the second case, acting independently, the surface postseismic displacements over six years are the sum of afterslip and viscoelastic processes simulated separately using the 3D model. The afterslip distribution on each node adopts a decay law as shown by aftershock seismicity in both cases (Agurto-Detzel et al., 2019; Bedford et al., 2016; Lange et al., 2014; Perfettini and Avouac, 2007). We find that the coupling with afterslip increases the total surface displacement by less than 6% (Fig. S5). Similar findings are presented by Freed et al. (2017) who investigated the postseismic deformation after the  $M_w$  9.0 2010 Tohoku earthquake in Japan. Therefore, we concluded that it is a reasonable approach to separately investigate the viscoelastic relaxation and afterslip contributions to the postseismic deformation.

#### 2.4. Rheological parameters of the five simulations of the forward model

For the four simulations PL1–PL4 with dislocation creep we assume that the rheology of the slab is controlled by diabase rock and the one of the oceanic upper mantle by the mineral olivine with 0.005 wt.% of water content because of their well-known rock composition and water content from a mid-ocean ridge basalt (MORB) source (Hirth and Kohlstedt, 1996). In simulation PL1 and PL2 we combine a wet quartzite for the continental crust with the two dislocation creep parameters for the continental mantle, that is wet olivine with 0.005 wt.% and 0.1 wt.% of water, respectively. In contrast, simulation PL3 and PL4 instead use a diabase for the continental crust and the same dislocation creep parameters for the continental mantle as simulations PL1 and PL2. Finally, in simulation LI5 we assume that the crust is linear elastic and that the postseismic relaxation in the upper mantle is controlled by linear viscoelasticity with a viscosity of  $1.3 \times 10^{19}$  Pa s in agreement to previous studies for the Chilean subduction zone (e.g. Bedford et al., 2016; Peña et al., 2019). The elastic and dislocation creep parameters of simulations and configuration of each simulation are presented in Table 1 and Table 2, respectively.

### 3. Results

In the following we present the results of five parameter sets of the forward model. Four of these use power-law rheology with dislocation creep (simulations PL1–PL4) and one uses a linear viscoelastic rheology (simulation LI5) as listed in Table 2. The inversion parameters used to produce all five afterslip distributions are identical.

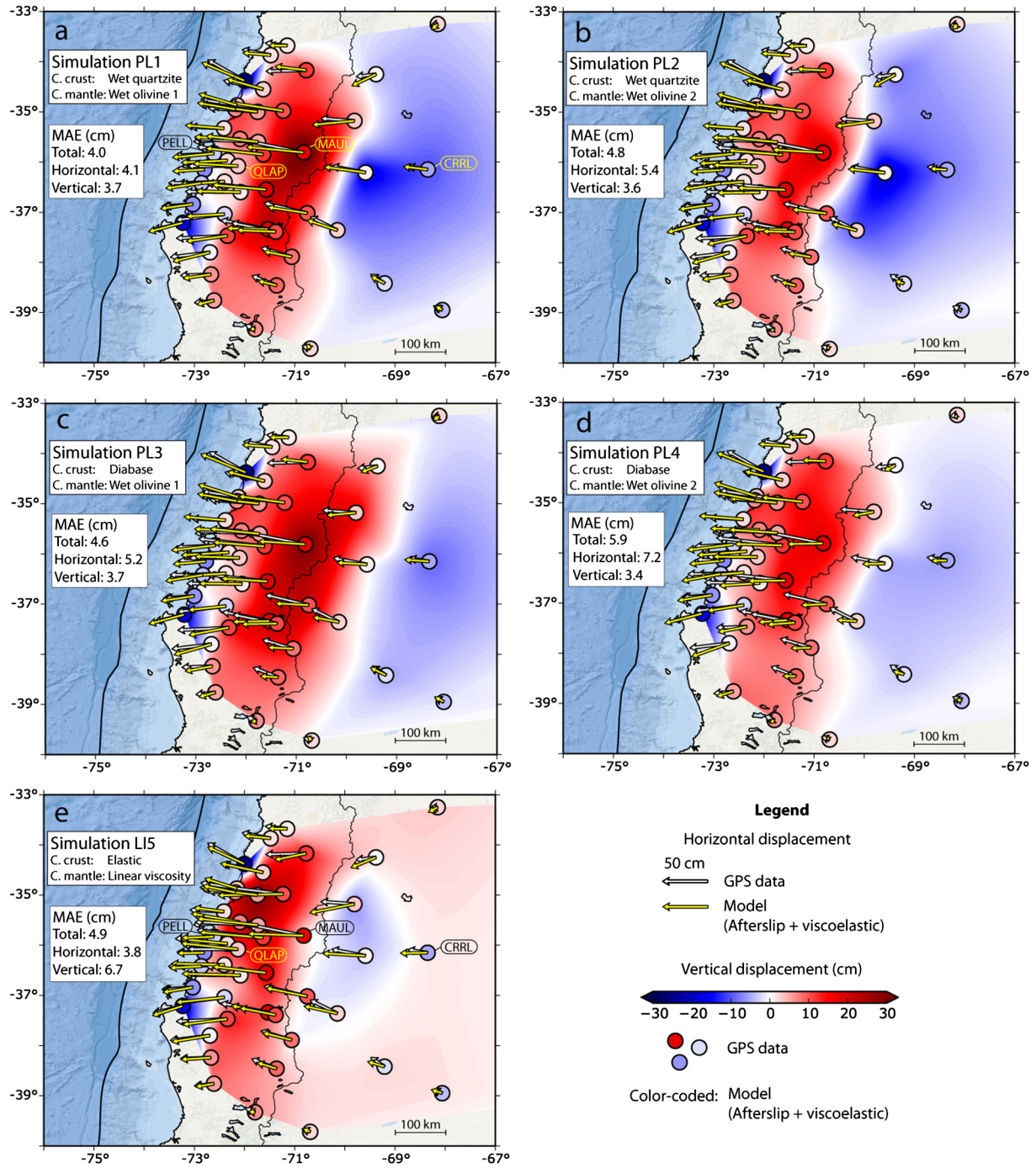
#### 3.1. Horizontal and vertical surface displacements

Fig. 4 shows for all five simulations the modelled displacement (the sum of the cumulative postseismic relaxation after six years and the inverted afterslip) and the observed displacement at the cGPS stations. The overall displacement patterns of the horizontal component are well captured by all simulations but larger discrepancies are found in the vertical component in the volcanic arc and back arc areas. Simulations PL1–PL4 using power-law rheology can

better explain the fast uplift in the volcanic arc and subsidence in the back arc than the linear rheology simulation LI5, which results in opposite patterns to the observed uplift at station MAUL in the middle and subsidence at station CRRL in the far fields. The change from the observed uplift to subsidence in the back arc is slightly better explained by simulation PL4, but the amplitude of the horizontal displacement is not well captured. Furthermore, the observed cumulative displacements on the coast line are well fitted by all simulations, suggesting that near-field observations are mainly dominated by afterslip processes as already pointed out by previous studies (e.g. Bedford et al., 2013; Qiu et al., 2018).

To quantify the deviations between model results and cGPS data, we calculate the Mean Absolute Error (MAE) for each simulation separately for the cumulative total, horizontal and vertical displacements after six years. The smallest MAE is achieved by simulation PL1 with 4.0 cm (Fig. 4a). Compared to simulation PL1 there is an increase of the total MAE of 20%, 15%, 48% and 23% for simulations PL2, PL3, PL4, and LI5, respectively. Interestingly there is a trade-off between the quality of the fit of the horizontal and the vertical cumulative displacements. For example, simulation PL4 (Fig. 4d) has the largest MAE with 5.9 cm, but the smallest error in the vertical (MAE=3.4 cm) and the largest error for the horizontal displacement (MAE=7.2 cm) while simulation LI5 can explain the horizontal displacement best (MAE=3.8 cm), but the vertical displacement has the worst fit (MAE=6.7 cm). The latter originates mainly from a poor fit to observed displacements at the cGPS stations located in the volcanic and back arcs (Fig. 4e).

We also investigate the main features in the surface displacement patterns over time by comparing simulation PL1, which has the lowest MAE with 4.0 cm in comparison to simulation LI5. To account for the temporal decay of afterslip, we applied a decay law for the afterslip with the shape of the aftershock seismicity decay. This is support by previous studies which found a good correlation between the temporal evolution of the afterslip and aftershock seismicity (Agurto-Detzel et al., 2019; Lange et al., 2014; Perfettini and Avouac, 2007). To gain insight into the main surface deformation differences between models with linear and non-linear rheology, in Fig. 5 we show and compare the time-series of four cGPS stations located in the near field (PELL), middle field (MAUL and QLAP) and far field (CRRL) with the combined results of the forward and inversion model. Additional time-series comparison is found in Fig. S6. We find that the largest differences are shown in the displacement rates. Even though the simulation with linear rheology can best explain the cumulative horizontal displacement (smallest MAE in the horizontal component), it does not reproduce convincingly the time-series of the postseismic displacements in the first years compared to simulation PL1 (Fig. 5 b–c and Fig. S6 f–i). This has also been shown by Freed and Bürgmann (2004) for the postseismic deformation associated to the 1992 Landers and 1999 Hector Mine earthquakes and Peña et al. (2019) for the Maule case. This is shown at cGPS stations QLAP and MAUL, where simulation LI5 underestimates the observed fast surface displacements, especially in the first two years.



**Fig. 4.** Observed versus modelled cumulative surface displacements after six years from the cGPS stations shown in Fig. 1. Only inland surface displacements are shown. MAE represents the Mean Absolute Error. The modelled surface displacement is the sum of the viscoelastic relaxation from the forward model and the resulting afterslip from the inversion.

### 3.2. Afterslip inversions

Fig. 6 shows the resulting afterslip distributions on the plate interface from the inversions of all five simulations. For power-law simulations PL1-PL4 the afterslip pattern is similar between 20–60 km depths except for changes in the amplitude. Simulation LI5 with linear rheology, however, shows a different pattern at these depths as we will present in this section. All simulations show afterslip maximums surrounding the maximum coseismic slip, which are regions of moderate coseismic slip. The maximum afterslip is located north of the maximum coseismic slip at 20 km depth in all simulations and reaches a maximum of  $\sim 3$  m for power-law rheol-

ogy simulations and 3.7 m for the simulation with linear rheology. The afterslip in the vicinity of the up-dip region of the megathrust fault is relatively small in all simulations; in zones of poor resolution (Figs. S7 and S8), no afterslip is resolved at  $<15$  km depth in simulation PL1 and small afterslip ( $<0.4$  m) at this region is apparent for the other simulations. Interestingly, all simulations show that the afterslip pattern is concentrated in two bands between  $34.5$ – $37.5^\circ\text{S}$  located at  $\sim 15$ – $30$  km and  $\sim 45$ – $60$  km depth. Nevertheless, the upper band from simulation LI5 is shallower ( $\sim 20$  km depth) and contains less afterslip compared to the same band from power-law rheology simulations ( $\sim 30$  km depth). These bands lie in zones of good resolution (Fig. S7), and can also be recov-



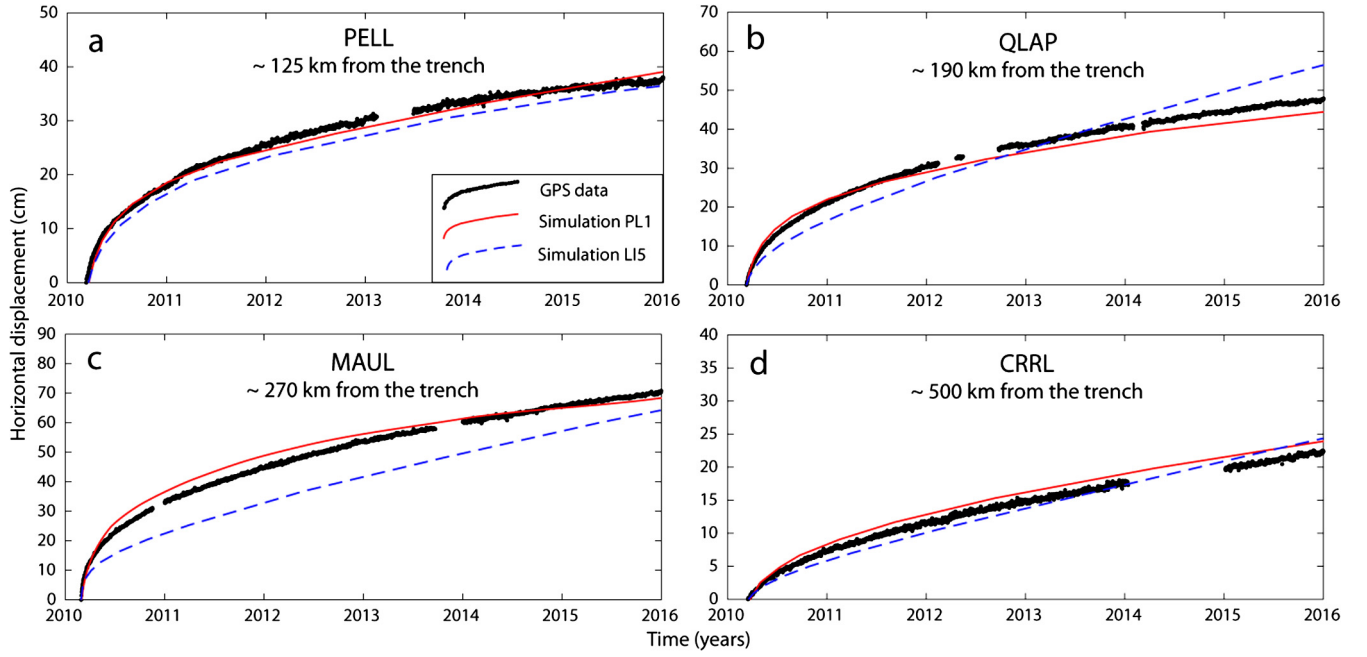


**Fig. 5.** Observed versus modelled time-series (daily solutions) of the horizontal surface displacements over six years after the main shock for cGPS stations PELL, QLAP, MAUL and CRRL. The effect of aftershocks, seasonal and interseismic loading (secular) are removed from the cGPS time-series observations. To account for the temporal decay of the modelled afterslip, we applied a decay law for the afterslip with the shape of the aftershock seismicity decay.

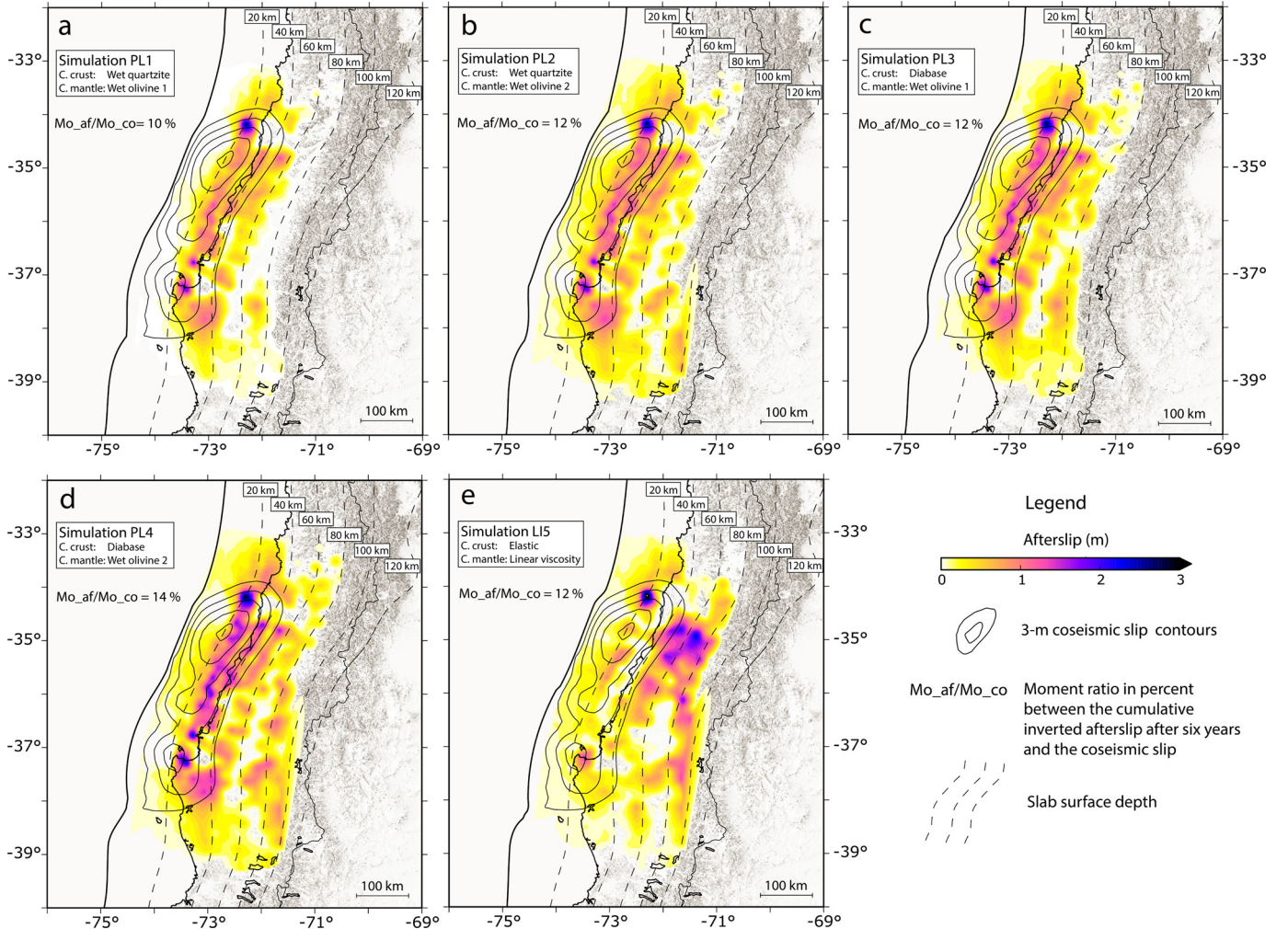


**Fig. 6.** Modelled cumulative afterslip distribution and residual displacement after six years. Ratio of afterslip moment release to coseismic moment release in percent ( $Mo_{af}/Mo_{co}$ ) associated to each simulation are also shown.

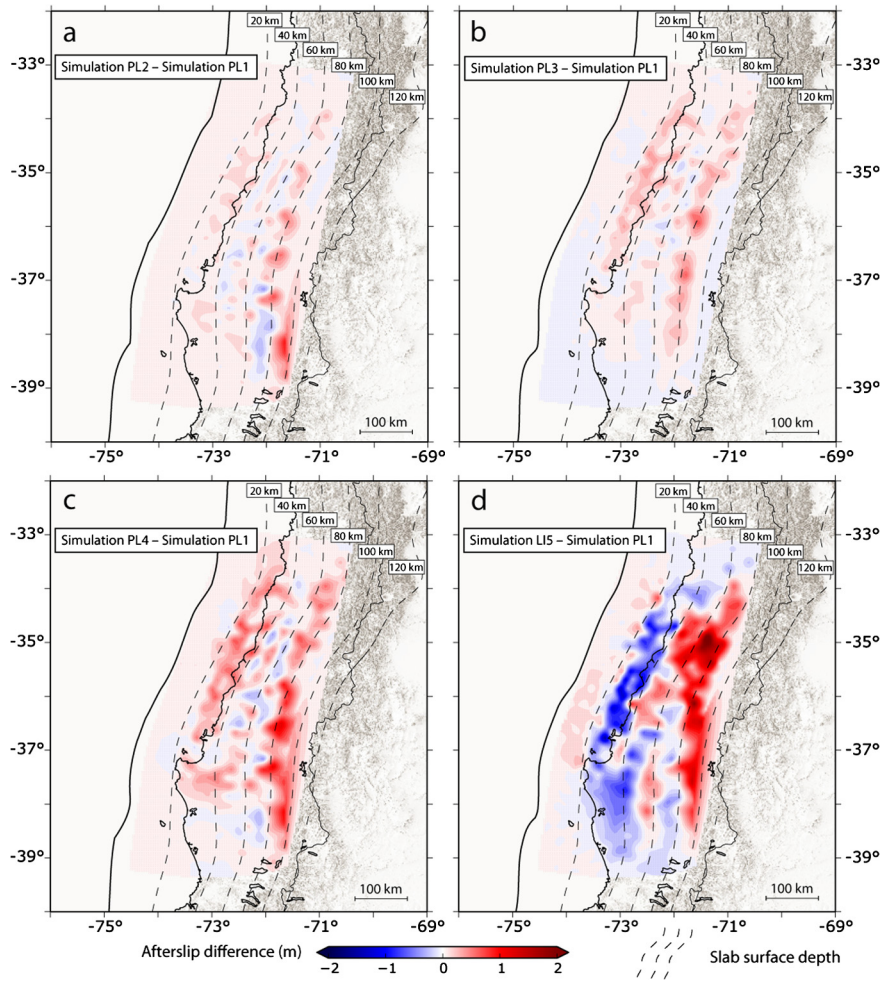


**Fig. 7.** Difference of afterslip distribution with respect to the results of the preferred simulation PL1. Note that the largest differences are found in the linear rheology simulation LI5.

ered from synthetic checkerboard tests (Fig. S8), further suggesting their plausibility. Furthermore, our tests show that the main pattern from these bands is apparent between a range of smoothing constants (Fig. S9). A deeper band at  $\sim 75$ – $90$  km depth is also exhibited more clearly in simulations PL3, PL4 and LI5. Despite these zones being at a lower resolution compared to the upper ones, they can still be well recovered as shown by our checkerboard test (Fig. S8a, b).

The main differences in afterslip distributions are found at greater depths between 60–90 km with two afterslip regions landward of the area of maximum coseismic slip at  $34.5$ – $36^\circ\text{S}$  and  $37$ – $38^\circ\text{S}$  (Figs. 6 and 7). In the north region, simulation LI5 shows the largest afterslip distribution which is localized in a region with up to 2.8 m between 70–90 km depths (Fig. 6e). For the same region, simulations PL3 and PL4 show afterslip up to 0.6 m and 0.8 m of magnitude (Fig. 6c, d) at  $\sim 80$  km depth, respectively. Simulation PL4 concentrates the highest afterslip of the power-law simulations at this depth (Fig. 6d). For the south region, the same simulations PL3 and PL4 show up to 0.9 m and 1.2 m at  $\sim 80$  km depth, respectively, and even deeper afterslip is shown from simulation LI5 which reaches up to 1.4 m at approximately 90 km depth (Fig. 6e).

In contrast, by analyzing the result at the same depths, the afterslip distributions from simulations PL1 and PL2 are reduced in magnitude (Fig. 6a–b). There is no deep afterslip for simulation PL1 in the north region (Fig. 6a), while simulation PL2 indicates up to

0.4 m (Fig. 6b). In the south region, the afterslip is reduced up to 0.5 m and 0.8 m for simulations PL1 and PL2, respectively.

To better visualize the differences of the afterslip inversion results, we show the differences relative to simulation PL1 as it achieves the smallest MAE (Fig. 7). The difference is increasing from power-law rheology simulations PL2–PL4 (Fig. 7a–c) reaching up to approximately 0.5 m and 1 m of afterslip in two bands along strike between 20–40 km and 60–90 km depth, respectively; the afterslip distribution difference between PL1 and LI5 is even larger showing differences not only in magnitude, but location as well. In particular, Fig. 7d shows that the shallower band of simulation LI5 decreases by approximately 1.5 m and increases in the vicinity of the trench by approximately 0.3 m between 10–20 km depth while in the deeper band, the afterslip distribution has a more pronounced amplitude that exceeds 2 m at 80 km depth.

## 4. Discussion

### 4.1. Discriminating afterslip distributions

Our best-fit result with the lowest MAE is simulation PL1 (Fig. 4a). However, the MAE of PL3 and LI5 is only 0.6 cm and 0.9 cm, respectively, larger; which is within the uncertainty of the data (7.5 cm). Therefore, we also use the spatial distribution and cumulative moment release from the aftershocks to test if one of these simulations fit better. According to Avouac (2015) and Perfettini and Avouac (2007), afterslip and aftershocks should spatially and temporally correlate. This has been shown by the good



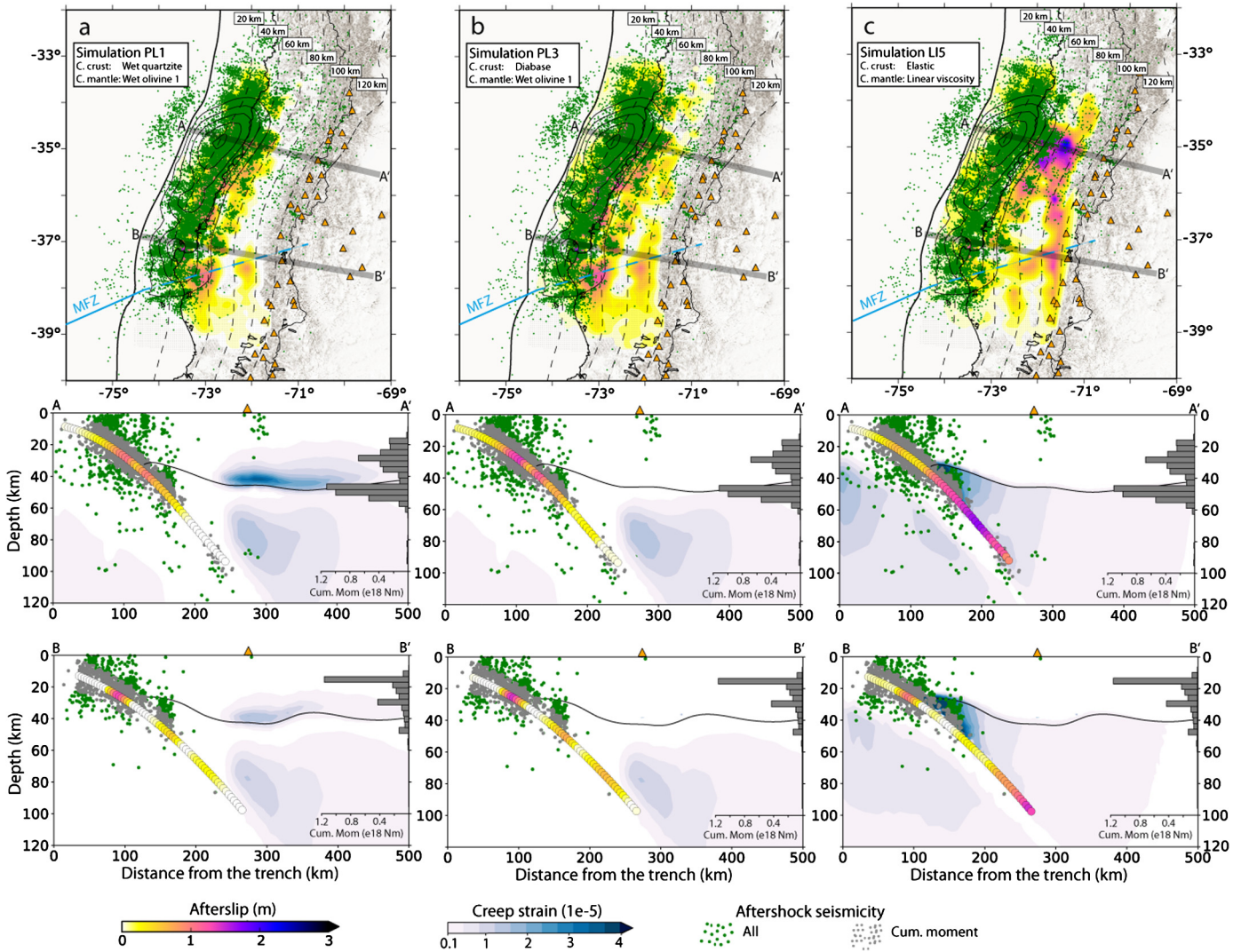


**Fig. 8.** Cumulative afterslip and aftershock seismicity after six years of the Maule event. a), b) and c) on top show the results of the afterslip inversion from simulations PL1, PL3 and LI5, respectively. Middle and lower panels show the cross-sections A-A' and B-B' with 25 km width associated to a), b) and c) with aftershock seismicity, afterslip, second invariant of the creep strain tensor and cumulative moment release of the aftershocks in the grey histograms. Aftershock seismicity is compiled from Lange et al. (2012), Rietbrock et al. (2012) and National Earthquake Information Center (NEIC-USGS). Lange et al. (2012) and Rietbrock et al. (2012) aftershock catalogues cover approximately from March to September in 2010. The periods (first days after the main shock and last 5 years) which are not covered for these catalogues are covered by NEIC. We exclude redundant events from the three catalogues. Histograms are calculated from the grey dots (aftershocks). To account for the uncertainties of the aftershock location, we calculate the cumulative moment release of the aftershocks as proposed by Rietbrock et al. (2012). We first select only aftershocks at  $\pm 10$  km distance from the interface geometry of the slab, and then we project the selected aftershocks on surface and calculate the cumulative moment release in windows of 10 km width. MFZ corresponds to the Mocha Fault Zone. Coseismic slip in black contours as shown in Fig. 6. Solid black line within figures depicts the Moho discontinuity.

correlation between aftershock seismicity and afterslip in studies of Agurto-Detzel et al. (2019), Lange et al. (2014), Perfettini and Avouac (2007) and Tassara et al. (2016) as well as by a study of Kato (2007) who shows that the aftershock triggering can be explained by afterslip. In addition, a mechanical afterslip-aftershock coupling may be also inferred from their temporal evolutions as both relaxation processes show almost the same decay law over time (Agurto-Detzel et al., 2019; Bedford et al., 2016; Hsu et al., 2006; Lange et al., 2014; Perfettini and Avouac, 2007).

In Fig. 8 we compare the resulting afterslip from models PL1, PL3 and LI5 with the location and accumulated moment release of the aftershocks. For the Maule case, most of the aftershock activity occurs in two belts: 1) a broad band equivalent to the megathrust failure during the Maule event, with most of aftershock activity outside of the maximum coseismic slip regions, but in regions of moderate coseismic slip (Agurto et al., 2012; Lange et al., 2012; Rietbrock et al., 2012), and 2) a slightly deeper one at approximately 50 km depth separated by a gap from the coseismic rupture do-

main. Strikingly, our afterslip inversions from power-law rheology simulations show a good spatial correlation with these aftershock belts, but less so in the linear rheology case (Fig. 8). These patterns are also reproduced to some extent by previous models. For example, the afterslip model of Lin et al. (2013) is sandwiched in between the upper and deeper aftershock belts. On the other hand, the afterslip model of Bedford et al. (2013) showed a better correlation with these aftershock belts, but not for the deeper segment ( $>60$  km). Similarly to a fully elastic crust, simulation PL3 that considers a strong material in the continental crust as diabase and simulation LI5 that considers a fully elastic continental crust result in deep afterslip, in contrast to the location of aftershock activity and its cumulative moment release (Fig. 8b-c). Conversely, simulation PL1 shows viscous deformation in the continental crust. It mostly occurs in its lower part at 25–45 km depth and beneath the volcanic arc at 220–450 km from the trench due to the implementation of weaker rock material (wet quartzite), which in turn compensates the deep afterslip (Fig. 8a). It is noteworthy to

point out that location of viscous deformation, apart from depending on dislocation creep parameters, strongly depends on rheology choice. The linear rheology simulation LI5 mostly concentrates the viscous deformation in the fore-arc continental mantle, while in the power-law rheology simulation PL3 it mostly occurs in the continental mantle beneath the volcanic arc. This difference may explain the larger afterslip at still 80–90 km depth from simulation LI5 as it tries to compensate the lack of deformation beneath the volcanic arc to explain the observed uplift.

Simulation PL1 has a better correlation with moment release from aftershock seismicity. It also results in a better agreement with frictional properties on the fault interface for the area associated to the postseismic deformation of the 2010 Maule event obtained from apparent locking degree from interseismic GPS velocities (Moreno et al., 2010), which is close to zero at >60 km depth, and with the depth-varying fault segmentation study from seismic wave radiation and seismicity of Lay et al. (2012). Therefore, we consider simulation PL1 as our preferred solution.

The assumption of a relatively weak lower crust is also supported by Farias et al. (2010) who suggested a low-viscosity ductile rather than a strong continental lower crust beneath the volcanic arc at 33.65°S based on seismicity and surface geology, in agreement to the location of the crustal weakening found in this study. This low-viscosity region may be controlled by partial melting as it has been shown from laboratory experiments that crustal rock strength could dramatically drop under melting conditions (Rosenberg and Handy, 2005). Rosenberg and Handy (2005) showed that a plausible melting of 12% for continental crustal rocks could drastically reduce the strength in amphibolite samples from ~1000 MPa to ~300 MPa (see Fig. 2 in Rosenberg and Handy, 2005). For the area associated to the postseismic deformation of the 2010 Maule event, previous studies from tomography images (González-Vidal et al., 2018) and magnetotelluric observations (Cordell et al., 2019) have illuminated potential melting regions, which are in good agreement with the location of the resulting viscous deformation in the continental lower crust.

Using similar data, but a different approach by also inverting for volumes of viscous strain in the continental lower crust and upper mantle, Weiss et al. (2019) found viscous deformation directly beneath the volcanic arc in the continental lower crust and mantle as well. However, our resulting cumulative maximum creep strain in six years in the continental lower crust is broader and it reaches a maximum of  $\sim 4 \times 10^{-5}$ , which is approximately four times larger than the one from them. Furthermore, they also find a region with a creep strain of  $\sim 8 \times 10^{-6}$  in the lithospheric mantle just beneath the Moho discontinuity between ~45–60 km depth, where we find smaller creep strain ( $< 2 \times 10^{-6}$ ). Nevertheless, at deeper regions in the upper mantle, our results agree better. Their creep strain region at 45–60 km depth compensates their smaller and more localized deformation in the continental lower crust compared to our findings, as well as it contributes significantly to the horizontal surface displacement field. These differences may potentially be because of weakening in this region of the upper mantle (45–60 km depth) due to secondary effects such as temperature anomalies or rock material differentiation, which are not included in the forward modelling. Weiss et al. (2019) showed that the ability to infer viscous strain in the continental lower crust and upper mantle is lower because of the decrease of cGPS stations in the volcanic and back arc. Therefore, a denser cGPS network in these regions may be used to assess better the relative contribution of relaxation processes occurring in the continental lower crust and upper mantle to the postseismic deformation field.

Comparing these findings to studies triggered by the postseismic deformation associated to the 2011 Tohoku-oki earthquake, a weak continental lower crust beneath the volcanic arc is also required to explain the postseismic cGPS observations (Hu et al.,

2014; Muto et al., 2016). Similarly, the joint inversion of afterslip and lower-crustal viscous strain from space geodetic observations have imaged low transient viscosities in the lower crust beneath the orogenic belt from GPS observations for the 1999 Chi-Chi earthquake (Tang et al., 2019) and the 2016 Kumamoto earthquake beneath active volcanoes from GPS and InSAR observations (Moore et al., 2017), suggesting that transient stress relaxation in the lower crust may be a common and key process following large earthquakes in actively orogenic or volcanic regions.

Our results also show that viscous deformation, due to dislocation creep processes, in the continental upper mantle is a key process during postseismic deformation, supporting previous studies such as Agata et al. (2019), Freed and Bürgmann (2004), and Qiu et al. (2018). Although the mantle rock composition is well known (Hirth and Kohlstedt, 2003), its water content may vary. These variations could be responsible for the small deep afterslip in the south region shown by simulation PL1, as higher water content would produce less deep afterslip, as shown by simulations PL1 and PL3 (0.1 wt.%) compared to simulations PL2 and PL4 (0.005 wt.%), respectively. In this context, this afterslip pattern might compensate the lack of higher water content. The southern region coincides with the Mocha Fracture Zone (MFZ) at the subducting oceanic crust (Contreras-Reyes et al., 2008, and light blue line in Fig. 8), suggesting a higher water content in the mantle wedge due to dehydration metamorphic reactions.

The assumption of homogeneous rock properties in the continental crust and upper mantle could also explain the residual displacements as well as secondary features in temperature anomalies in the volcanic and back arcs as pointed out by Peña et al. (2019) for the Maule case. Furthermore, although our test suggests that afterslip and viscoelastic processes can be modelled independently, there may be localized effects. Agata et al. (2019) have recently showed that afterslip-viscoelastic relaxation coupling could locally increase at some inland cGPS stations the surface displacements in ~10% in the horizontal component and ~30% in the vertical using a stress-driven afterslip model, but the total surface displacement field does not substantially change (see Fig. 8 in Agata et al., 2019). On the other hand, the effect of the coupling on afterslip is most important at >60 km depth (almost zero at <60 km depth, see Muto et al., 2019), which will not considerably affect our results since most of the afterslip occurs at <60 km depth in our preferred simulation. However, a future joint non-linear inversion or an afterslip driven model could elucidate secondary features such as temperature anomalies, rock material heterogeneities and afterslip-viscoelastic interaction for the Maule case.

#### 4.2. Afterslip models and moment release

As shown in the previous section, the choice of the rheology (linear or power-law) has a strong impact on the afterslip magnitude and pattern, in particular at greater depths (Figs. 6 and 7). It also has an impact on the location and magnitude of the postseismic viscoelastic relaxation (Fig. 8). This deep afterslip pattern for the Maule case was first investigated by Klein et al. (2016) through a deep and weak subduction channel. However, in contrast to their findings, we propose that non-linear viscoelastic relaxation processes in the continental lower crust may result in a surface deformation pattern similar to that expected from a deep subduction channel. Nevertheless, we do not neglect that both processes may operate together as they cannot be separated unambiguously from the observed postseismic surface displacements.

In the shallower segment at <30 km depth, the afterslip model of Klein et al. (2016) reaches up to ~9 m during the first year of postseismic deformation. Similar patterns have recently been shown by Weiss et al. (2019) who found up to 8 m of afterslip at ~10 km depth over the first six years. In contrast, our

results suggest that afterslip mostly occurs at 20–60 km depths. These differences might be because Weiss et al. (2019) constrain afterslip to preferentially occur in the regions surrounding the coseismic slip patches. Here, Weiss et al. (2019) considered the slip model of Lin et al. (2013), which results in small slip at <10 km depth. In contrast, other slip models as the one used in this study (Moreno et al., 2012) and Yue et al. (2014) show more slip at shallower regions, but all differ to some extent. These differences are mainly produced because of the fault geometry and data considered during the inversion approach. We have evaluated the impact of slip on our results (Fig. S10). They show that the location and magnitude of the main afterslip patterns remain almost the same between 20–60 km depth, with small variations at shallower and greater depths. In particular, we cannot precisely assess these differences at shallower regions as they are poorly constrained due to the lack of offshore observations. Hence, offshore cGPS stations may be used in future as a proxy to better constrain the relative contribution of postseismic relaxation processes to the surface observations and the competing models, since our preferred afterslip model differs mostly from the one of Klein et al. (2016) and Weiss et al. (2019) in the shallower region (<20 km depth).

At other subduction zones, afterslip inversions show similar deep pattern from models considering only viscoelasticity for upper mantle (Qiu et al., 2018; Tsang et al., 2016; Yamagiwa et al., 2015). This assumption results in an increase of afterslip in the up-dip and reduction in the deeper segments (Qiu et al., 2018; Sun et al., 2014; Tsang et al., 2016). However, these models generally still result in moderate deep afterslip distribution at 80 km depth as the models of Qiu et al. (2018) and Tsang et al. (2016) for the Sumatra-Andaman region by considering a jointly inversion for afterslip and viscoelastic heterogeneities in the asthenosphere above an elastic 100-km-thick lithosphere. The viscoelastic relaxation from these setups occurs in the mantle wedge at 100 km depth and at 250–400 km from the trench. In our preferred simulation most of the viscoelastic relaxation also occurs at such distances from the trench, but conversely, it occurs in a much shallower region, i.e., in the lower crust at approximately 45 km depth (Fig. 8a). Since the fact of differences in data source and coverage, jointly inversion and slab geometry and age, we speculate that such a still deep afterslip may be due to the lack of shallower viscoelastic relaxation.

The moment released by the cumulative afterslip after six years is in our simulations considerably smaller in comparison to fully elastic models. Lin et al. (2013) estimated a moment of  $3.6\text{--}5.1 \times 10^{21}$  Nm in 1.3 years following the 2010 Maule earthquake, which is 20–30% of the seismic moment from the main shock. Similar results were reported in other subduction zones after megathrust earthquakes using fully elastic models (e.g. Hsu et al., 2006; Perfettini et al., 2010) and from models that assume a linear viscoelastic mantle rheology as the one from Yamagiwa et al. (2015) who found ~21% of the ratio of afterslip to the coseismic moment release after 2.5 years of postseismic deformation associated to the Tohoku-oki earthquake. In contrast, we estimate a moment release of  $1.8 \times 10^{21}$  Nm in six years from our preferred afterslip distribution which is equivalent to 10% of the coseismic moment (Fig. 6a). Thus, in comparison to a power-law rheology simulation that allows viscoelastic relaxation in the continental lower crust, afterslip distribution on the plate interface is larger by a factor of approximately two from models that assume an elastic crust above a mantle with linear viscoelastic rheology. This is mainly explained by the location of the viscoelastic relaxation as a model that allows non-linear viscoelastic relaxation in a shallower region as the continental lower crust reduces the afterslip, in particular and considerably at greater depths.

## 5. Conclusions

We use a 3D forward model with power-law rheology with dislocation creep in the crust and upper mantle and linear viscoelastic rheology to investigate the first six years of postseismic relaxation after the 2010 Maule earthquake. From the residual displacements, we derive afterslip distributions through a standard inversion scheme. Our results show that the largest differences of afterslip distributions are located in the deeper segment of the fault interface at depths >60 km.

Given that the Mean Absolute Error (MAE) between the cumulative observed and modelled displacements of PL1, PL3 and LI5 is close to each other, we use the assumed correlation between afterslip and moment release from aftershock seismicity to further assess the model results. We find that our preferred simulation PL1 with the lowest MAE also correlates better to the accumulated aftershock moment release.

In comparison to the model with linear rheology, simulation PL1 shows especially in the first years of postseismic deformation a significantly better fit of the observed transient relaxation signal at the cGPS stations. The viscoelastic relaxation from our preferred simulation PL1 mainly occurs in the continental lower crust and to lesser extent in the upper mantle, both beneath the volcanic arc due to dislocation creep processes. In contrast, in the simulation with linear rheology, relaxation mainly occurs in the continental upper mantle beneath the fore arc. In particular, the non-linear viscoelastic relaxation in the continental lower crust trades off the deep afterslip and may be associated with partial melting. Therefore, our results suggest that the continental lower crust is weak rather than strong. We conclude that non-linear viscoelastic relaxation processes in the continental lower crust along with cumulative moment release by aftershocks might potentially better constrain afterslip inversions following megathrust earthquakes, particularly its maximum depth.

## Declaration of competing interest

The authors declare that they have no known competing financial interests or personal relationships that could have appeared to influence the work reported in this paper.

## Acknowledgements

Carlos Peña would like to thank the scholarship granted to him by both the German Academic Exchange Service (DAAD) and the National Commission for Scientific and Technological Research (CONICYT-Becas Chile). Marcos Moreno acknowledges support from FONDECYT 1181479, the Millennium Nucleus NC160025, ANILLO ACT192169, and CONICYT/FONDAP 15110017. This work has received funding from the Initiative and Networking Fund of the Helmholtz Association through the project “Advanced Earth System Modelling Capacity (ESM)”. All data used are properly cited in the reference list, figures, and tables. We would like to thank the Editor Jean-Philippe Avouac, Sylvain Barbot and one anonymous reviewer for their insightful and constructive comments and suggestions.

## Appendix A. Supplementary material

Supplementary material related to this article can be found online at <https://doi.org/10.1016/j.epsl.2020.116292>.

## References

- Agata, R., Barbot, S.D., Fujita, K., Hyodo, M., Iinuma, T., Nakata, R., Ichimura, T., Hori, T., 2019. Rapid mantle flow with power-law creep explains deformation after



- the 2011 Tohoku mega-quake. *Nat. Commun.* 10 (1), 1385. <https://doi.org/10.1038/s41467-019-08984-7>.
- Aguirre, L., Bataille, K., Novoa, C., Peña, C., Vera, F., 2019. Kinematics of subduction processes during the earthquake cycle in Central Chile. *Seismol. Res. Lett.* 90 (5), 1779–1791. <https://doi.org/10.1785/0220180391>.
- Agurto, H., Rietbrock, A., Ryder, I., Miller, M., 2012. Seismic-afterslip characterization of the 2010 Mw 8.8 Maule, Chile, earthquake based on moment tensor inversion. *Geophys. Res. Lett.* 39, L20303. <https://doi.org/10.1029/2012GL053434>.
- Agurto-Detzel, H., Font, Y., Charvis, P., Régnier, M., Rietbrock, A., Ambrois, D., Courboux, F., 2019. Ridge subduction and afterslip control aftershock distribution of the 2016 Mw 7.8 Ecuador earthquake. *Earth Planet. Sci. Lett.* 520, 63–76. <https://doi.org/10.1016/j.epsl.2019.05.029>.
- Avouac, J.-P., 2015. From geodetic imaging of seismic and aseismic fault slip to dynamic modeling of the seismic cycle. *Annu. Rev. Earth Planet. Sci.* 43, 233–271. <https://doi.org/10.1146/annurev-earth-060614-105302>.
- Barbot, S., 2018. Asthenosphere flow modulated by megathrust earthquake cycles. *Geophys. Res. Lett.* 45, 6018–6031. <https://doi.org/10.1029/2018GL078197>.
- Bedford, J., Moreno, M., Baez, J.C., Lange, D., Tilmann, F., Rosenau, M., Heidbach, O., Oncken, O., Bartsch, M., Rietbrock, A., Tassara, A., Bevis, M., Vigny, C., 2013. A high-resolution, time-variable after slip model for the 2010 Maule Mw = 8.8, Chile megathrust earthquake. *Earth Planet. Sci. Lett.* 383, 26–36. <https://doi.org/10.1016/j.epsl.2013.09.020>.
- Bedford, J., Moreno, M., Li, S., Oncken, O., Baez, J.C., Bevis, M., Heidbach, O., Lange, D., 2016. Separating rapid relocking, afterslip, and viscoelastic relaxation: an application of the postseismic straightening method to the Maule 2010 cGPS. *J. Geophys. Res., Solid Earth* 121, 7618–7638. <https://doi.org/10.1002/2016JB013093>.
- Bevis, M., Brown, A., 2014. Trajectory models and reference frames for crustal motion geodesy. *J. Geod.* 88 (3), 283–311.
- Blewitt, G., Hammond, W.C., Kreemer, C., 2018. Harnessing the GPS data explosion for interdisciplinary science. *Eos* 99. <https://doi.org/10.1029/2018EO104623>.
- Carter, N.L., Kirby, S.H., 1978. Transient creep and semi brittle behavior of crystalline rocks. *Pure Appl. Geophys.* 116, 807–839. <https://doi.org/10.1007/BF00876540>.
- Chopra, P.N., 1997. High-temperature transient creep in olivine rocks. *Tectonophysics* 279, 93–111. [https://doi.org/10.1016/S0040-1951\(97\)00134-0](https://doi.org/10.1016/S0040-1951(97)00134-0).
- Christensen, N., 1996. Poisson's ratio and crustal seismology. *J. Geophys. Res.* 101 (B2), 3139–3156. <https://doi.org/10.1029/95JB03446>.
- Contreras-Reyes, E., Grevemeyer, I., Flueh, E.R., Reichert, C., 2008. Upper lithospheric structure of the subduction zone offshore of southern Arauco peninsula, Chile, at ~38 S. *J. Geophys. Res., Solid Earth* 113 (B7). <https://doi.org/10.1029/2007JB005569>.
- Cordell, D., Unsworth, M.J., Diaz, D., Reyes-Wagner, V., Currie, C.A., Hicks, S.P., 2019. Fluid and melt pathways in the central Chilean subduction zone near the 2010 Maule earthquake (35°–36°S) as inferred from magnetotelluric data. *Geochem. Geophys. Geosyst.* 20, 1818–1835. <https://doi.org/10.1029/2018GC008167>.
- Fariás, M., Comte, D., Charrier, R., Martinod, J., David, C., Tassara, A., Tapia, F., Fock, A., 2010. Crustal-scale structural architecture in central Chile based on seismicity and surface geology: implications for Andean mountain building. *Tectonics* 29, TC3006. <https://doi.org/10.1029/2009TC002480>.
- Freed, A.M., Bürgmann, R., 2004. Evidence of power-law flow in the Mojave Desert mantle. *Nature* 430 (6999), 548. <https://doi.org/10.1038/nature02784>.
- Freed, A.M., Hirth, G., Behn, M.D., 2012. Using short-term postseismic displacements to infer the ambient deformation conditions of the upper mantle. *J. Geophys. Res.* 117, B01409. <https://doi.org/10.1029/2011JB008562>.
- Freed, A.M., Hashima, A., Becker, T.W., Okaya, D.A., Sato, H., Hatanaka, Y., 2017. Resolving depth-dependent subduction zone viscosity and afterslip from post-seismic displacements following the 2011 Tohoku-oki, Japan earthquake. *Earth Planet. Sci. Lett.* 459, 279–290. <https://doi.org/10.1016/j.epsl.2016.11.040>.
- González-Vidal, D., Obermann, A., Tassara, A., Bataille, K., Lupi, M., 2018. Crustal model of the Southern Central Andes derived from ambient seismic noise Rayleigh-wave tomography. *Tectonophysics* 744, 215–226. <https://doi.org/10.1016/j.tecto.2018.07.004>.
- Hayes, G., Wald, D., Johnson, R., 2012. Slab1.0: a three-dimensional model of global subduction zone geometries. *J. Geophys. Res., Solid Earth* 117 (B1), B01302. <https://doi.org/10.1029/2011JB008524>.
- Hergert, T., Heidbach, O., 2006. New insights in the mechanism of postseismic stress relaxation exemplified by the June 23rd 2001 Mw = 8.4 earthquake in southern Peru. *Geophys. Res. Lett.* 33 (L02307). <https://doi.org/10.1029/2005GL024585>.
- Hirth, G., Kohlstedt, D., 2003. Rheology of the upper mantle and the mantle wedge: a view from the experimentalists. In: *Inside the Subduction Factory*, pp. 83–105.
- Hirth, G., Kohlstedt, D.L., 1996. Water in the oceanic upper mantle: implications for rheology, melt extraction and the evolution of the lithosphere. *Earth Planet. Sci. Lett.* 144 (1–2), 93–108. [https://doi.org/10.1016/0012-821X\(96\)00154-9](https://doi.org/10.1016/0012-821X(96)00154-9).
- Hsu, Y.J., Simons, M., Avouac, J.P., Galetzka, J., Sieh, K., Chlieh, M., Natawidjaja, D., Prawirodirdjo, L., Bock, Y., 2006. Frictional afterslip following the 2005 Nias-Simeulue earthquake, Sumatra. *Science* 312 (5782), 1921–1926. <https://doi.org/10.1126/science.1126960>.
- Hu, Y., Bürgmann, R., Freymueller, J., Banerjee, P., Wang, K., 2014. Contributions of poroelastic rebound and a weak volcanic arc to the postseismic deformation of the 2011 Tohoku earthquake. *Earth Planets Space* 66 (1), 106. <https://doi.org/10.1186/1880-5981-66-106>.
- Kato, N., 2007. Expansion of afterslip areas caused by propagating post-seismic sliding. *Geophys. J. Int.* 168 (2), 797–808. <https://doi.org/10.1111/j.1365-246X.2006.03255.x>.
- Klein, E., Fleitout, L., Vigny, C., Garaud, J.D., 2016. Afterslip and viscoelastic relaxation model inferred from the large-scale postseismic deformation following the 2010 Mw 8.8 Maule earthquake (Chile). *Geophys. J. Int.* 205 (3), 1455–1472. <https://doi.org/10.1093/gji/ggw086>.
- Lambert, V., Barbot, S., 2016. Contribution of viscoelastic flow in earthquake cycles within the lithosphere-asthenosphere system. *Geophys. Res. Lett.* 43, 10,142–10,154. <https://doi.org/10.1002/2016GL070345>.
- Lange, D., Tilmann, F., Barrientos, S.E., Contreras-Reyes, E., Methe, P., Moreno, M., Heit, B., Agurto, H., Bernard, P., Vilotte, J.-P., Beck, S., 2012. Aftershock seismicity of the 27 February 2010 Mw 8.8 Maule earthquake rupture zone. *Earth Planet. Sci. Lett.* 317–318, 413–425. <https://doi.org/10.1016/j.epsl.2011.11.034>.
- Lange, D., Bedford, J., Moreno, M., Tilmann, F., Baez, J., Bevis, M., Krueger, F., 2014. Comparison of postseismic afterslip models with aftershock seismicity for three subduction-zone earthquakes: Nias 2005, Maule 2010 and Tohoku 2011. *Geophys. J. Int.* 199 (2), 784–799. <https://doi.org/10.1093/gji/ggu292>.
- Lay, T., Kanamori, H., Ammon, C.J., Koper, K.D., Hutko, A.R., Ye, L., Rushing, T.M., 2012. Depth-varying rupture properties of subduction zone megathrust faults. *J. Geophys. Res., Solid Earth* 117 (B4). <https://doi.org/10.1029/2011JB009133>.
- Li, S., Moreno, M., Bedford, J., Rosenau, M., Heidbach, O., Melnick, D., Oncken, O., 2017. Postseismic uplift of the Andes following the 2010 Maule earthquake: Implications for mantle rheology. *Geophys. Res. Lett.* 44, 1768–1776. <https://doi.org/10.1002/2016GL071995>.
- Li, S., Wang, K., Wang, Y., Jiang, Y., Dosso, S.E., 2018. Geodetically inferred locking state of the Cascadia megathrust based on a viscoelastic Earth model. *J. Geophys. Res., Solid Earth* 123, 8056–8072. <https://doi.org/10.1029/2018JB015620>.
- Lin, Y.N., Sladen, A., Ortega-Culaciati, F., Simons, M., Avouac, J.-P., Fielding, E.J., Brooks, B.A., Bevis, M., Genrich, J., Rietbrock, A., Vigny, C., Smalley, R., Socquet, A., 2013. Coseismic and postseismic slip associated with the 2010 Maule Earthquake, Chile: characterizing the Arauco Peninsula barrier effect. *J. Geophys. Res., Solid Earth* 118 (6), 3142–3159. <https://doi.org/10.1002/jgrb.50207>.
- Loveless, J.P., Meade, B.J., 2010. Geodetic imaging of plate motions, slip rates, and partitioning of deformation in Japan. *J. Geophys. Res.* 115, B02410. <https://doi.org/10.1029/2008JB006248>.
- Masterlark, T., 2003. Finite element model predictions of static deformation from dislocation sources in a subduction zone: sensitivities to homogeneous, isotropic, Poisson-solid, and half-space assumptions. *J. Geophys. Res., Solid Earth* 108 (B11). <https://doi.org/10.1029/2002JB002296>.
- Masuti, S., Barbot, S., Karato, S., Feng, L., Banerjee, P., 2016. Upper-mantle water stratification inferred from observations of the 2012 Indian Ocean earthquake. *Nature* 538, 373–377. <https://doi.org/10.1038/nature19783>.
- Métrois, M., Socquet, A., Vigny, C., 2012. Interseismic coupling, segmentation and mechanical behavior of the central Chile subduction zone. *J. Geophys. Res., Solid Earth* 117 (B3). <https://doi.org/10.1029/2011JB008736>.
- Moore, J.D.P., Yu, H., Tang, C.-H., Wang, T., Barbot, S., Peng, D., Masuti, S., Dauwels, J., Hsu, Y.-J., Lambert, V., Nanjundiah, P., Wei, S., Lindsey, E., Feng, L., Shibasaki, B., 2017. Imaging the distribution of transient viscosity after the 2016 Mw 7.1 Kumamoto earthquake. *Science* 356 (6356), 163–167. <https://doi.org/10.1126/science.aal3422>.
- Moreno, M., Rosenau, M., Oncken, O., 2010. 2010 Maule earthquake slip correlates with pre-seismic locking of Andean subduction zone. *Nature* 467 (7312), 198–202. <https://doi.org/10.1038/nature09349>.
- Moreno, M., Melnick, D., Rosenau, M., Baez, J., Klotz, J., Oncken, O., Tassara, A., Chen, J., Bataille, K., Bevis, M., Socquet, A., Bolte, J., Vigny, C., Brooks, B., Ryder, I., Grund, V., Smalley, B., Carrizo, D., Bartsch, M., Hase, H., 2012. Toward understanding tectonic control on the Mw 8.8 2010 Maule Chile earthquake. *Earth Planet. Sci. Lett.* 321–322, 152–165. <https://doi.org/10.1016/j.epsl.2012.01.006>.
- Muto, J., Shibasaki, B., Iinuma, T., Ito, Y., Ohta, Y., Miura, S., Nakai, Y., 2016. Heterogeneous rheology controlled postseismic deformation of the 2011 Tohoku-Oki earthquake. *Geophys. Res. Lett.* 43 (10), 4971–4978. <https://doi.org/10.1002/2016GL068113>.
- Muto, J., Moore, J.D.P., Barbot, S., Iinuma, T., Ohta, Y., Iwamori, H., 2019. Coupled afterslip and transient mantle flow after the 2011 Tohoku earthquake. *Sci. Adv.* 5 (9), eaaw1164. <https://doi.org/10.1126/sciadv.aaw1164>.
- Oleskevich, D.A., Hyndman, R.D., Wang, K., 1999. The updip and downdip limits to great subduction earthquakes: thermal and structural models of Cascadia, south Alaska, SW Japan, and Chile. *J. Geophys. Res.* 104 (B7), 14965–14991. <https://doi.org/10.1029/1999JB900060>.
- Peña, C., Heidbach, O., Moreno, M., Bedford, J., Ziegler, M., Tassara, A., Oncken, O., 2019. Role of lower crust in the postseismic deformation of the 2010 Maule earthquake: insights from a model with power-law rheology. *Pure Appl. Geophys.* 176, 3913–3928. <https://doi.org/10.1007/s00024-018-02090-3>.
- Perfettini, H., Avouac, J.P., 2007. Modeling afterslip and aftershocks following the 1992 Landers earthquake. *J. Geophys. Res., Solid Earth* 112 (B7). <https://doi.org/10.1029/2006JB004399>.
- Perfettini, H., Avouac, J.-P., Tavera, H., Kositsky, A., Nocquet, J.-M., Bondoux, F., Chlieh, M., Sladen, A., Audin, L., Farber, D.L., Soler, P., 2010. Seismic and aseismic slip on the central Peru megathrust. *Nature* 465 (7294), 78–81. <https://doi.org/10.1038/nature09062>.

- Qiu, Q., Moore, J.D.P., Barbot, S., Feng, L., Hill, E.M., 2018. Transient rheology of the Sumatran mantle wedge revealed by a decade of great earthquakes. *Nat. Commun.* 9 (995). <https://doi.org/10.1038/s41467-018-03298-6>.
- Ranalli, G., 1997. Rheology and deep tectonics. *Ann. Geofis.* XL (3), 671–780. <https://doi.org/10.4401/ag-3893>.
- Rebischung, P., Griffiths, J., Ray, J., Schmid, R., Collilieux, X., Garayt, B., 2012. IGS08: the IGS realization of ITRF2008. *GPS Solut.* 16 (4), 483–494. <https://doi.org/10.1007/s10291-011-0248-2>.
- Rietbrock, A., Ryder, I., Hayes, G., Haberland, C., Comte, D., Roecker, S., Lyon-Caen, H., 2012. Aftershock seismicity of the 2010 Maule Mw= 8.8, Chile, earthquake: correlation between co-seismic slip models and aftershock distribution? *Geophys. Res. Lett.* 39 (8). <https://doi.org/10.1029/2012GL051308>.
- Rollins, C., Barbot, S., Avouac, J., 2015. Postseismic deformation following the 2010 Mw=7.2 El Mayor-Cucapah earthquake: observations, kinematic inversions, and dynamic models. *Pure Appl. Geophys.* 172, 1305–1358. <https://doi.org/10.1007/s00024-014-1005-6>.
- Rosenberg, C., Handy, M., 2005. Experimental deformation of partially melted granite revisited: implications for the continental crust. *J. Metamorph. Geol.* 23 (1), 19–28. <https://doi.org/10.1111/j.1525-1314.2005.00555.x>.
- Rousset, B., Barbot, S., Avouac, J.-P., Hsu, Y.-J., 2012. Postseismic deformation following the 1999 Chi-Chi earthquake, Taiwan: implication for lower-crust rheology. *J. Geophys. Res.* 117, B12405. <https://doi.org/10.1029/2012JB009571>.
- Scholz, C.H., 1988. The brittle-plastic transition and the depth of seismic faulting. *Geol. Rundsch.* 77, 319–328. <https://doi.org/10.1007/BF01848693>.
- Shi, Q., Barbot, S., Wei, S., et al., 2020. Structural control and system-level behavior of the seismic cycle at the Nankai Trough. *Earth Planets Space* 72, 27. <https://doi.org/10.1186/s40623-020-1145-0>.
- Sun, T., Wang, K., Iinuma, T., Hino, R., He, J., Fujimoto, H., Kido, M., Osada, Y., Miura, S., Ohta, Y., Hu, Y., 2014. Prevalence of viscoelastic relaxation after the 2011 Tohoku-oki earthquake. *Nature* 514 (7520), 84–87. <https://doi.org/10.1038/nature13778>.
- Tang, C.-H., Hsu, Y.-J., Barbot, S., Moore, J.D., Chang, W.-L., 2019. Lower-crustal rheology and thermal gradient in the Taiwan orogenic belt illuminated by the 1999 Chi-Chi earthquake. *Sci. Adv.* 5 (2). eaav3287. <https://doi.org/10.1126/sciadv.aav3287>.
- Tassara, A., Götze, H.J., Schmidt, S., Hackney, R., 2006. Three-dimensional density model of the Nazca plate and the Andean continental margin. *J. Geophys. Res., Solid Earth* 111 (B9). <https://doi.org/10.1029/2005JB003976>.
- Tassara, A., Soto, H., Bedford, J., Moreno, M., Baez, J.C., 2016. Contrasting amount of fluids along the megathrust ruptured by the 2010 Maule earthquake as revealed by a combined analysis of aftershocks and afterslip. *Tectonophysics* 671, 95–109. <https://doi.org/10.1016/j.tecto.2016.01.009>.
- Tsang, L.L.H., Hill, E.M., Barbot, S., Qiu, Q., Feng, L., Hermawan, I., Banerjee, P., Natawidjaja, D.H., 2016. Afterslip following the 2007 Mw 8.4 Bengkulu earthquake in Sumatra loaded the 2010 Mw 7.8 Mentawai tsunami earthquake rupture zone. *J. Geophys. Res., Solid Earth* 121, 9034–9049. <https://doi.org/10.1002/2016JB013432>.
- Vigny, C., Socquet, A., Peyrat, S., Ruegg, J.-C., Mtois, M., Madariaga, R., Morvan, S., Lancieri, M., Lacassin, R., Campos, J., Carrizo, D., Bejar-Pizarro, M., Barrientos, S., Armijo, R., Aranda, C., Valderas-Bermejo, M.-C., Ortega, I., Bondoux, F., Baize, S., Lyon-Caen, H., Pavez, A., Vilotte, J.P., Bevis, M., Brooks, B., Smalley, R., Parra, H., Baez, J.-C., Blanco, M., Cimbaro, S., Kendrick, E., 2011. The 2010 Mw 8.8 Maule mega-thrust earthquake of Central Chile, monitored by GPS. *Science* 332, 1417–1421. <https://doi.org/10.1126/science.1204132>.
- Völker, D., Grevemeyer, I., Stipp, M., Wang, K., He, J., 2011. Thermal control of the seismogenic zone of southern central Chile. *J. Geophys. Res.* 116 (B10). <https://doi.org/10.1029/2011JB008247>.
- Wada, I., He, J., Hasegawa, A., Nakajima, J., 2015. Mantle wedge flow pattern and thermal structure in Northeast Japan: effects of oblique subduction and 3-D slab geometry. *Earth Planet. Sci. Lett.* 426, 76–88. <https://doi.org/10.1016/j.epsl.2015.06.021>.
- Wang, K., Hu, Y., He, J., 2012. Deformation cycles of subduction earthquakes in a viscoelastic Earth. *Nature* 484 (7394), 327–332. <https://doi.org/10.1038/nature11032>.
- Weiss, J.R., Qiu, Q., Barbot, S., Wright, T.J., Foster, J.H., Saunders, A., Erickson, T.L., 2019. Illuminating subduction zone rheological properties in the wake of a giant earthquake. *Sci. Adv.* 5 (12). eaax6720. <https://doi.org/10.1126/sciadv.aax6720>.
- Yamagiwa, S., Miyazaki, S., Hirahara, K., Fukahata, Y., 2015. Afterslip and viscoelastic relaxation following the 2011 Tohoku-oki earthquake (Mw9.0) inferred from inland GPS and seafloor GPS/Acoustic data. *Geophys. Res. Lett.* 42 (1), 66–73. <https://doi.org/10.1002/2014GL061735>.
- Yue, H., Lay, T., Rivera, L., An, C., Vigny, C., Tong, X., Báez Soto, J.C., 2014. Localized fault slip to the trench in the 2010 Maule, Chile Mw= 8.8 earthquake from joint inversion of high-rate GPS, teleseismic body waves, InSAR, campaign GPS, and tsunami observations. *J. Geophys. Res., Solid Earth* 119 (10), 7786–7804. <https://doi.org/10.1002/2014JB011340>.